

Graphene Decorated with ZnO Nanocrystals with Improved Electrochemical Properties Prepared by a Facile In Situ Hydrothermal Route

Wen-Tao Song, Jian Xie^{*}, Shuang-Yu Liu, Yun-Xiao Zheng, Gao-Shao Cao, Tie-Jun Zhu, Xin-Bing Zhao

Department of Materials Science and Engineering, Zhejiang University, Hangzhou 310027, China

*E-mail: xiejian1977@zju.edu.cn

Received: 3 December 2011 / Accepted: 11 February 2012 / Published: 1 March 2012

Graphene anchored with nanocrystal ZnO was synthesized by a facile in situ one-pot hydrothermal route. The nanocomposite was characterized by X-ray diffraction (XRD), Raman spectra (RS), X-ray photoelectron spectroscopy (XPS), thermogravimetric analysis (TGA), scanning electron spectroscopy (SEM), and transmission electron microscopy (TEM). The electrochemical properties of the nanocomposite were investigated by galvanostatic cycling and cyclic voltammetry (CV). It was found that ZnO particles with a size of around 30-40 nm are homogeneously anchored on graphene due to the interaction between the precursors. A layered structure has formed by the alternating stacking of graphene sheets and ZnO nanoparticles. The electrochemical tests showed that the ZnO/graphene nanocomposite yields an initial charge capacity of 420 mAh g⁻¹, and that the nanocomposite exhibits an obviously improved cycling stability compared to bare ZnO because of the buffering, confining and conducting effects of the incorporated graphene. Electrochemical impedance spectroscopy (EIS) was used to understand the effect of graphene on the electrochemical properties of nanocrystal ZnO.

Keywords: ZnO, graphene, nanocomposite, electrochemical properties, anode material

1. INTRODUCTION

To meet ever increasing high-capacity and high-power requirements for Li-ion batteries, a considerable attention has been given to the lithium-metal alloys. Tin-based materials have received a special interest because they can yield a much higher capacity (990 mAh g⁻¹ for metallic Sn) than carbon-based materials by forming a maximum Li_{4.4}Sn composition at room temperature [1, 2]. However, these materials showed rapid capacity fade due to the large volume changes (358%) during the Li-alloying/de-alloying processes. Similar to Sn, Zn also showed a Li-storage ability by forming

various Li-Zn alloys [2, 3]. It can yield a capacity of around 410 mAh g^{-1} with the formation of a LiZn composition, higher than the theoretical value (372 mAh g^{-1}) of carbon materials. In addition, the Li-alloying/de-alloying reactions of Zn occur in an appropriate potential range of 0 to 0.5 V. Among the Zn-based materials, ZnO is a typical one which showed a potential application as anode for Li-ion batteries [4–6].

The capacity fade of ZnO upon repeated cycling, however, still occurs due to the intrinsic volume changes. Previous reports showed that a stable cycling could be achieved by using nanostructured ZnO materials [7, 8]. Another effective method to improve the cycling stability of ZnO is to form mixed oxides such as ZnCo_2O_4 [9], ZnFe_2O_4 [10], and ZnV_2O_4 [11]. The nanosized transition metal formed during the lithiation process was considered to be responsible for the good cycling stability of these mixed oxides. Forming a composite with a metal [12] or oxides [13, 14] of Li-inert or with less volume changes was also proved to be a useful measure to alleviate the volume changes. In this regard, carbon materials [15, 16] are more suitable to be used as matrices because they not only contribute to the over capacity but also increase the electric conductivity, in addition to the buffering effect.

Compared with other carbon materials, graphene, a flat monolayer of sp^2 -bonded carbon atoms [17], is also a promising matrix due to its unique characteristics such as large specific surface area [18], high mechanical strength [19], and high electronic conductivity [20]. The research on SnO_2 [21–27] and FeSb_2 [28] has shown that its electrochemical properties could be remarkably enhanced by loading it onto graphene.

Previous work has shown that graphene was also an ideal support for ZnO to improve its capacitive behavior [29]. The effect of graphene on the electrochemical Li-storage properties of ZnO has not been reported yet. In this work, a ZnO/graphene nanocomposite was synthesized by a facile in situ hydrothermal route and the effect of graphene on the electrochemical performance of ZnO was investigated.

2. EXPERIMENTAL SECTION

2.1 Preparation of ZnO/graphene

Graphite oxide (30 mg), which was prepared by a modified Hummer's method [30], was added into 60 mL of deionized (DI) water with sonication for 3 h to form a homogeneous dispersion. Then, 3 mmol of $\text{Zn}(\text{NO}_3)_2 \cdot 6\text{H}_2\text{O}$ was added to the above dispersion with pH adjusted to 8 using ammonia water (25 % wt).

After sonication again, the solution was transferred to a Teflon-lined stainless steel autoclave (100 mL) and heated in an electric oven at $150 \text{ }^\circ\text{C}$ for 10 h. The resulting product was separated by centrifugation, washed with DI water and dried at $60 \text{ }^\circ\text{C}$ under vacuum for 8 h. The product is named ZnO/G, where G represents graphene. A control experiment was performed to prepare bare ZnO using the same route without adding graphite oxide.

2.2 Materials Characterization

The crystalline phases of the obtained products were identified by X-ray diffraction (XRD) on a Rigaku D/Max-2550pc powder diffractometer equipped with Cu K α radiation ($\lambda = 1.541 \text{ \AA}$). X-ray photoelectron spectroscopy (XPS) measurements were performed on a KRATOS AXIS ULTRA-DLD spectrometer with a monochromatic Al K α radiation ($h\nu = 1486.6 \text{ eV}$). The morphologies of the products were observed by field emission scanning electron microscopy (FE-SEM) on a FEI-sirion microscope and transmission electron microscopy (TEM) on a JEM 2100F microscope. Raman spectra were collected on a Jobin-Yvon Labor Raman HR-800 Raman system using a 514.5 nm Ar-ion laser at 10 mW. N $_2$ absorption/desorption isotherms were recorded on an AUTOSORB-1-C apparatus. Thermogravimetric analysis (TGA) was conducted on a DSCQ1000 instrument from 45 to 650 °C at a ramp rate of 10 °C min $^{-1}$ in air.

2.3 Electrochemical measurements

The electrochemical performance of the hydrothermal products (ZnO/G, and ZnO) was measured using CR2025-type coin cells. The hydrothermal product, polyvinylidene fluoride (PVDF) and acetylene black with a weight ratio of 75:15:10 were sufficiently mixed in N-methyl pyrrolidone (NMP) with magnetic stirring to form electrode slurry. The working electrodes were made by spreading the slurry onto Ni foam and dried at 100 °C under vacuum overnight. The half cells were assembled in an Ar-filled glove box using Li foil as the counter electrode and polypropylene microporous film (Celgard 2300) as the separator. The electrolyte used was 1 M LiPF $_6$ dissolved in ethylene carbonate (EC)/dimethyl carbonate (DMC) (1:1 in volume). Galvanostatic cycling of the cells was conducted on a Neware BTS-5V10mA battery cycler (Shenzhen, China) at 0.05-2 V (vs. Li/Li $^+$). Cyclic voltammetry (CV) test was carried out on an Arbin BT2000 system in the voltage range 0.05–2.0 V (vs. Li/Li $^+$) at 0.1 mV s $^{-1}$. Electrochemical impedance spectroscopy (EIS) measurements were conducted on a CHI660C electrochemistry workstation by applying an ac voltage of 5 mV amplitude over the frequency range from 10 $^{-2}$ to 10 5 Hz at de-lithiated states. All of the electrochemical measurements were performed at 25 °C.

3. RESULTS AND DISCUSSION

Fig. 1(a) shows the XRD patterns of the hydrothermal products. All the diffraction peaks can be indexed to wurtzite structure of ZnO (space group $P6_3mc$, JCPDS no. 80-0075) for both the samples. No diffraction peaks related to carbon can be detected, implying that the reduced graphene oxide sheets are completely exfoliated due to the loading of the ZnO particles on their surfaces. The Raman spectra of ZnO and ZnO/G are presented in Fig. 1(b). For ZnO/G, two bands appear at 1350 and 1580 cm $^{-1}$, corresponding to the disordered (D) band and graphitic (G) band of carbon materials [31]. The peak at around 440 cm $^{-1}$ corresponds to E_2 (high) mode [32, 33], which is the characteristic peak of the hexagonal wurtzite phase [34]. Note that the intensity of this peak is remarkably reduced in

ZnO/G compared to that in bare ZnO due possibly to the interaction between ZnO and graphene. The peak at 582 cm^{-1} is assigned to E_1 (LO) mode associated with the structural defects in ZnO [35, 36]. The bands located at near 330 and 1130 cm^{-1} are due to the multiple-phonon scattering processes [34]. The XRD and Raman spectra clearly confirm the formation of wurtzite-type ZnO and the presence of carbon in ZnO/G.

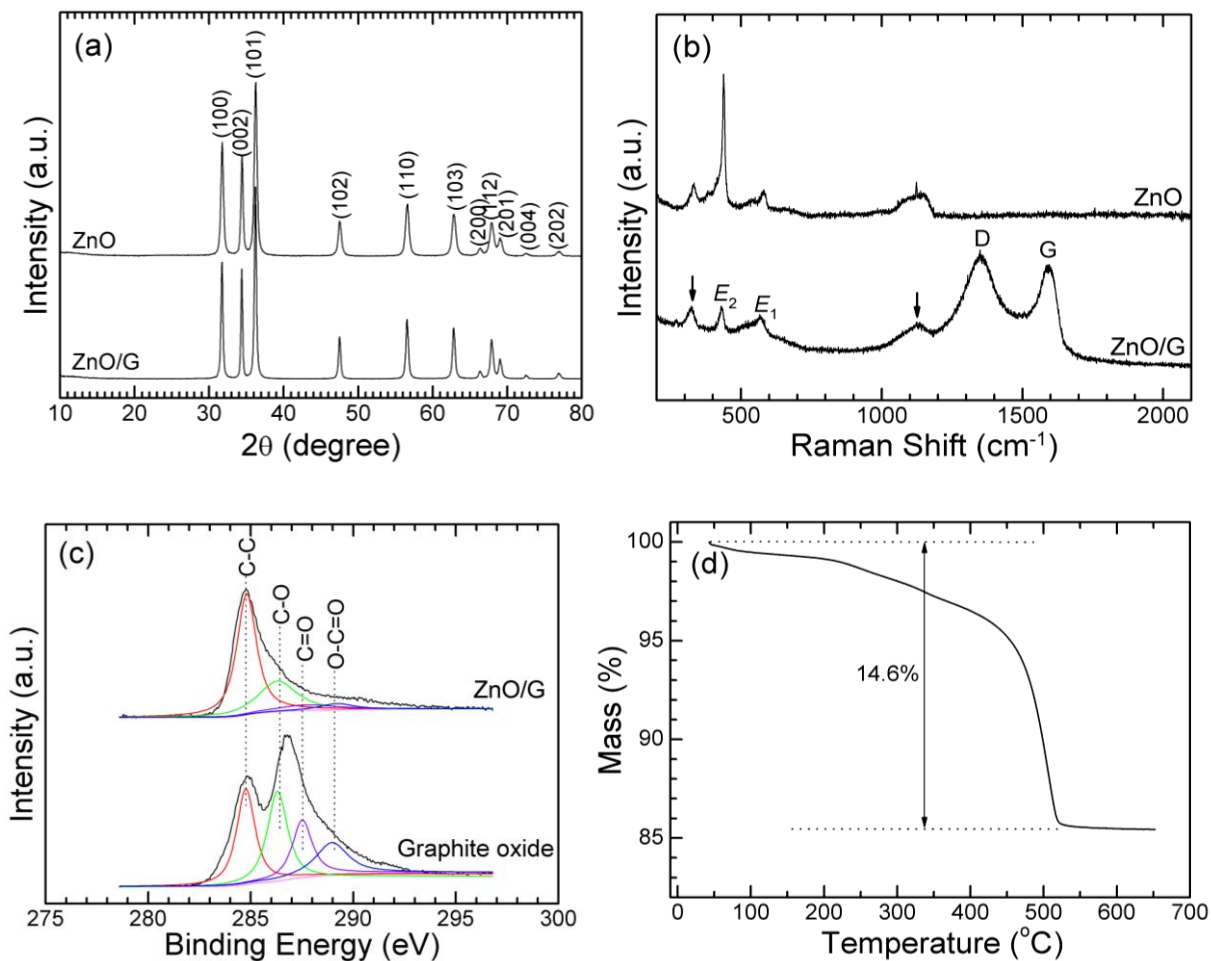


Figure 1. (a) XRD patterns of ZnO/G and ZnO, (b) Raman spectra of ZnO/G and ZnO, (c) C 1s XPS of ZnO/G and graphite oxide, and (d) TGA of ZnO/G.

Fig. 1(c) compares the C1s XPS of graphite oxide and ZnO/G. The XPS can be fitted into four peaks, corresponding to carbon atoms in different functional groups: sp^2 carbon (C-C, 284.8 eV), carbon in C-O bonds (286.3 eV), carbonyl carbon (C=O, 287.6 eV) and carboxylate carbon (O-C=O, 289.0 eV) [37, 38]. Note that the peak intensity of the oxygen-bonded carbons (C-O, C=O and O-C=O) was considerably reduced in ZnO/G, indicating a sufficient reduction of graphite oxide into graphene during the hydrothermal process. It should be noted that the product still contains residual epoxide and/or hydroxyl groups evidenced from the remained C-O peak, which is consistent with the theoretical calculation that these groups are difficult to remove when located at the edges of the

graphite oxide [39]. The graphene content in ZnO/G is determined by TGA as seen in Fig. 1(d). According to TGA, the weight percentage of graphene in ZnO/G is 14.6%.

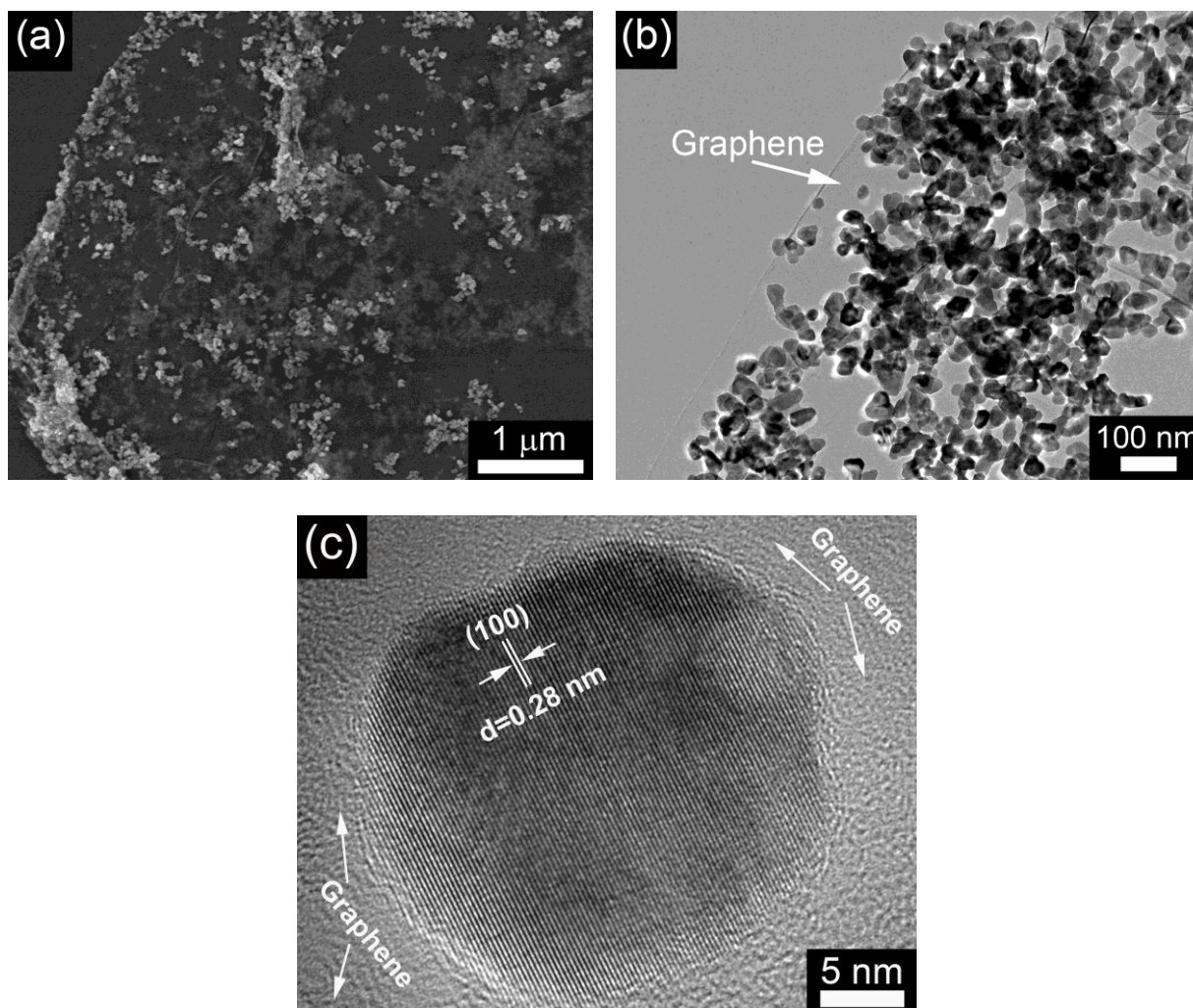


Figure 2. (a) SEM, (b) TEM and (c) HRTEM images of ZnO/G.

Fig. 2(a) displays a typical SEM image of a ZnO/G flake. From the transparent graphene, it is evident that the ZnO nanoparticles are confined in graphene. The transparent nature of the graphene implies that it is fully exfoliated into single or few-layer sheet, agreeing well with the XRD results. Fig. 2(b) shows a TEM image of the ZnO/G nanocomposite. Obviously, nanosized ZnO particles are uniformly anchored on graphene. The quasi-spheric ZnO particles exhibit a narrow size distribution of around 30-40 nm. It should be stressed that almost all the ZnO nanoparticles are attached on graphene. The electrostatic attraction between the positively charged Zn^{2+} and the negatively charged graphene oxide sheets [40] in the precursors plays a crucial role in the firm attachment of the ZnO particles on graphene in the final product.

The HRTEM image of an individual ZnO particle on graphene is demonstrated in Fig. 2(c). The fringe spacing is measured to be 0.28 nm, consistent with the lattice spacing of (100) plane of

ZnO. The HRTEM image also indicates a good crystallization of ZnO, in agreement with the XRD results. It can be concluded based on the above analyses that a ZnO/graphene hybrid nanostructure has formed during this in situ one-pot hydrothermal process. The formation mechanism of the hybrid nanostructure is schematically illustrated in Fig. 3.

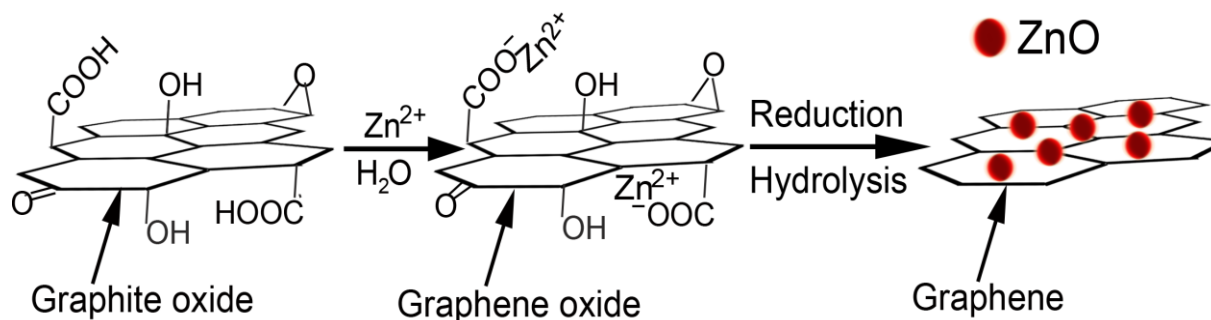


Figure 3. Formation mechanism of the ZnO/G hybrid nanostructure.

It suggests that the electrostatic attraction between the precursors is responsible for the homogeneous attachment of ZnO nanoparticles on graphene. The anchored nanoparticles, in turn, prevent the restacking of the hydrophobic graphene. On the other hand, without the confinement by the graphene sheets, the ZnO nanoparticles tend to aggregate as indicated in Fig. 4.

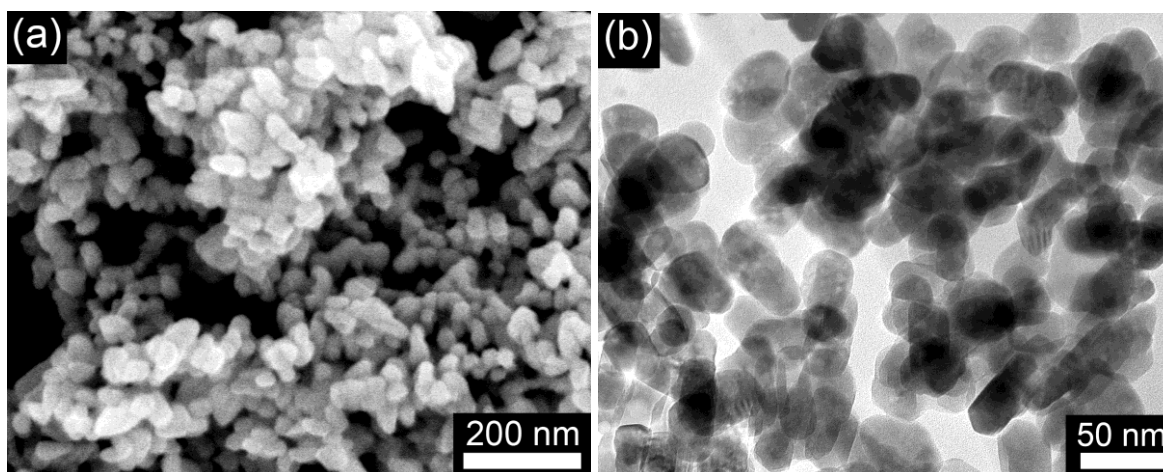
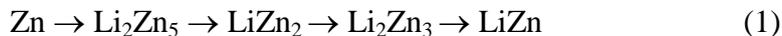


Figure 4. (a) SEM and (b) TEM images of bare ZnO nanoparticles.

Fig. 5(a) shows the charge-discharge curves of ZnO/G for the initial three cycles. The first discharge (Li-insertion) and charge (Li-extraction) capacities of the nanocomposite are 1235 and 420 mAh g^{-1} , respectively. Note that ZnO/G exhibits a large first irreversible capacity due to the reduction decomposition of the electrolyte and the formation of the solid state interface (SEI) layer. In addition, the graphene with a large irreversible capacity [41] also contributes to the observed large irreversible capacity of the nanocomposite. The first charge capacity is close to the theoretical value (410 mAh g^{-1})

of ZnO when a LiZn composition is formed. Similar capacity was observed in the previous work [4]. As seen in Fig. 5a, successive potential plateaus are observed, which are related to Li-alloying/dealloying processes of Zn. The possible phase transitions during the Li-insertion process can be written as [2, 3]:



After the first cycle, reversible electrochemical reactions take place evidenced from the almost overlapped charge or discharge curves.

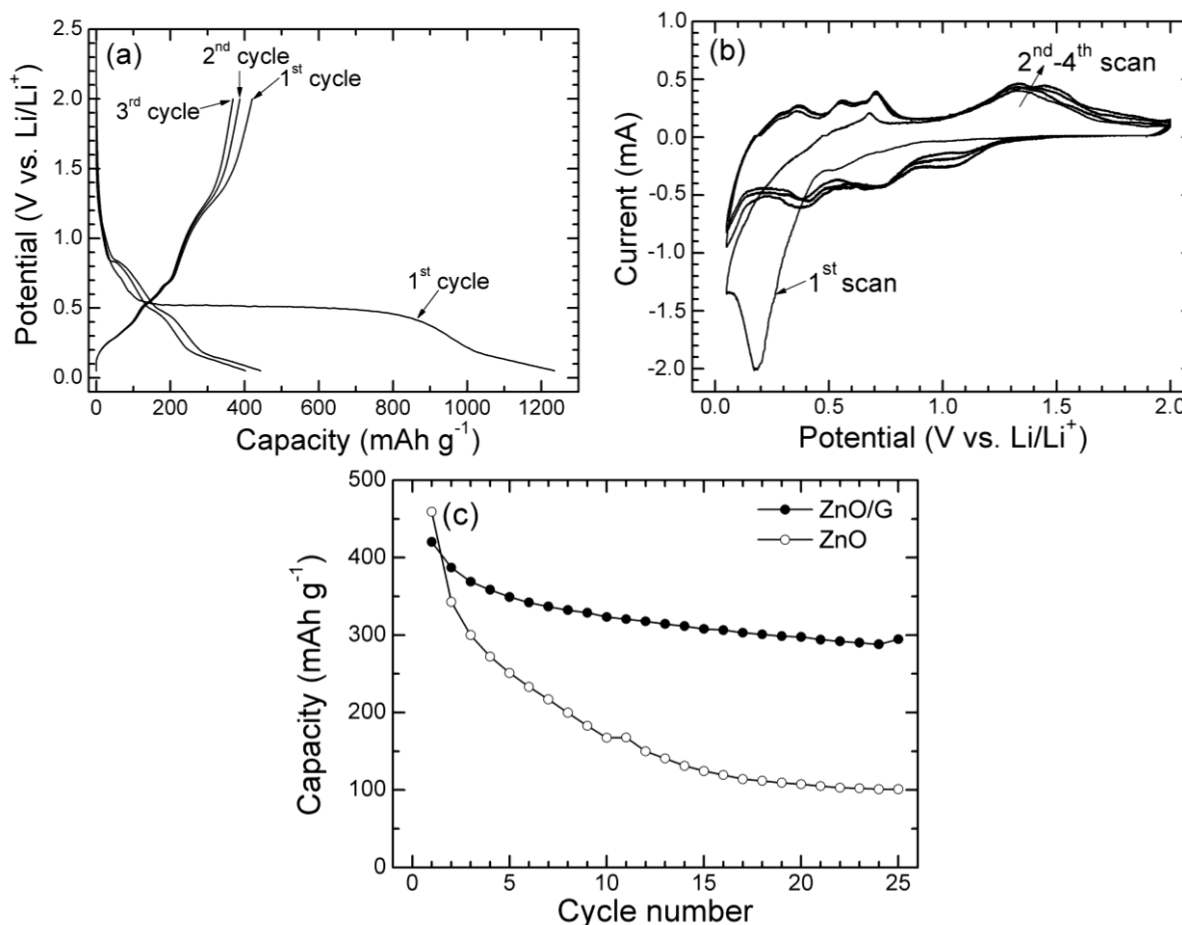


Figure 5. Electrochemical properties of the hydrothermal products: (a) charge-discharge curves of ZnO/G at 50 mA g⁻¹, (b) CV plots of ZnO/G at 0.1 mV s⁻¹, and (c) comparison of cycling stability between bare ZnO and ZnO/G at 50 mA g⁻¹.

Fig. 5(b) presents the CV plots of ZnO/G scanned at 0.1 mV s⁻¹. During the first scan, an extremely large reduction peak is evident at about 0.2 V, which corresponds to the long potential plateau in the first discharge curve. During the subsequent scans, the reduction and oxidation peaks, associated with the Li-alloying/dealloying processes, are almost fixed at given positions between 0 and 1.5 V, suggesting a good electrochemical reversibility. Fig. 5(c) compares the cycling stability between

ZnO/G and bare ZnO. It is apparent that ZnO/G exhibits an enhanced cycling stability compared to bare ZnO. After 25 cycles, ZnO/G keeps a capacity close to 300 mAh g^{-1} . In contrast, the capacity of bare ZnO drops rapidly to 101 mAh g^{-1} after the same cycles. The improvement in cycling stability can be ascribed to the incorporated graphene which not only buffers the large volume changes and but also restrains the aggregation of the ZnO nanoparticles. In addition, the two-dimensional (2D) conductive network constructed by graphene also contributes to the improved cycling stability by enhancing the electrochemical reaction kinetics. Furthermore, the large specific area of graphene maximizes the contact of active material with the electrolyte, increasing the electrode kinetics.

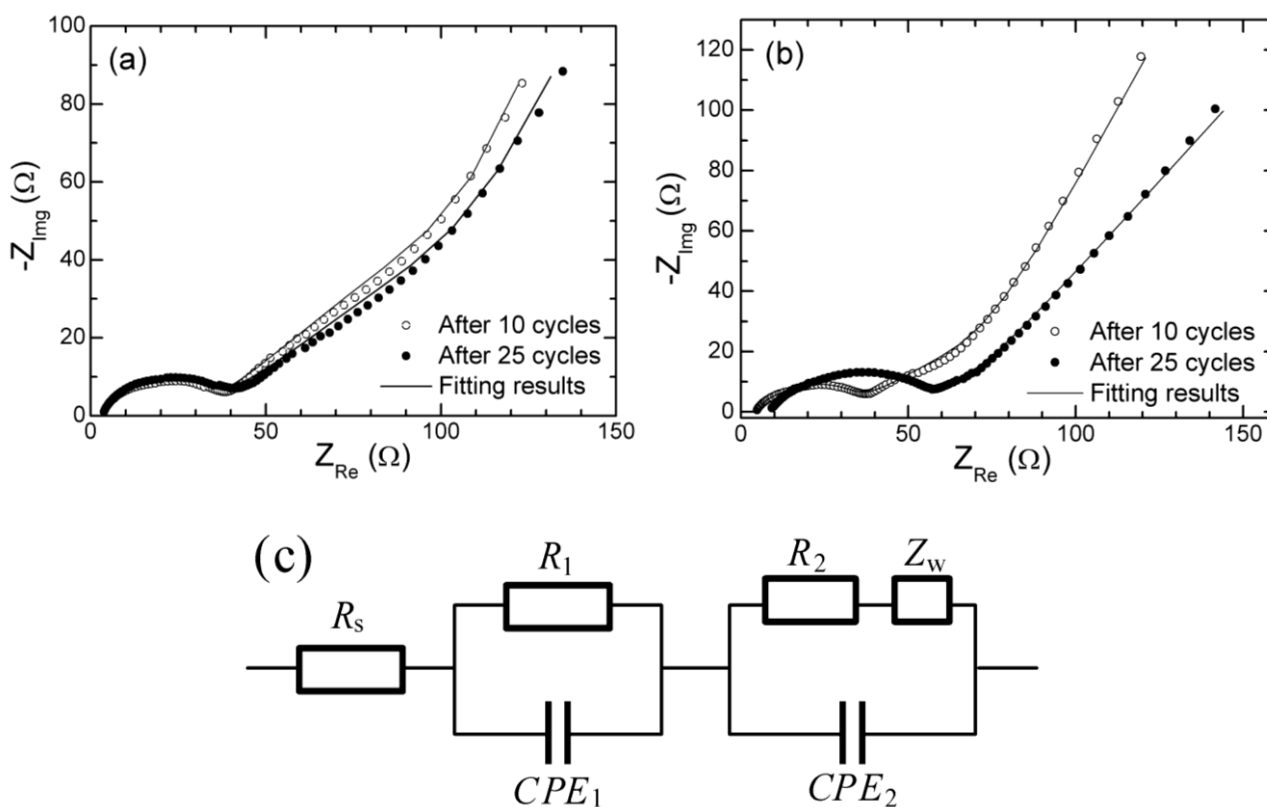


Figure 6. Nyquist plots of (a) ZnO/G and (b) bare ZnO after 5 and 25 cycles, and (c) equivalent circuit for the Nyquist plots.

To understand the different electrochemical behaviors between ZnO/G and bare ZnO, EIS measurements were carried out after the electrodes have been cycled for 5 and 25 times. The Nyquist plots in Fig. 6(a), (b) are composed of two partially overlapped semicircles and a sloping line. The first semicircle in the high-frequency region is correlated to Li-ion diffusion through the SEI layer, the second semicircle in the middle-frequency region corresponds to the charge transfer resistance of the electrochemical reactions, and the sloping line in the low-frequency region is related to solid state diffusion of Li-ion in the bulk electrode [42]. The Nyquist plots are fitted by the equivalent circuit given in Fig. 6(c), where R_s represents electrolyte resistance, R_1 and CPE_1 denote SEI layer resistance and the corresponding capacitance, R_2 and CPE_2 are the charge transfer resistance and the double layer

capacitance, and R_w is the bulk diffusion resistance.

Note that all the plots are well fitted by the equivalent circuit. The fitting results are summarized in Table 1. Due to the dispersion effect, a constant phase element (CPE) instead of a capacitor (C) is used in this work. The CPE can be expressed as [43]:

$$Y_{CPE} = Y_c \omega^n \cos(n\pi/2) + jY_c \omega^n \sin(n\pi/2) \quad (2)$$

Where $\omega (=2\pi f, f$ is the frequency) is the angular frequency and $j = (-1)^{1/2}$. As shown in Table 1, the ZnO/G electrode exhibits a much smaller change in R_s than the ZnO electrode during cycling, indicative of a negligible change in the electrolyte. The ZnO/G electrode also shows a slight change in R_1 , suggesting that the SEI layer is stable upon repeated cycling. The stabilization of the SEI layer is possibly due to the confinement of the ZnO nanoparticles by the graphene sheets. By contrast, the reduction in R_1 for the ZnO electrode means that the microstructure of the electrode undergoes significant changes, during which the original SEI layers were destroyed possibly accompanied by the formation of new ones. A slight change of R_2 is also observed for ZnO/G, which implies that a stable electrode/electrolyte interface has been established. The confining of the nanoparticles by graphene accounts probably for the stabilized electrode/electrolyte interface. For bare ZnO, on the contrary, the aggregation and pulverization of the nanoparticles upon prolonged cycling lead to the sluggish electrochemical reaction kinetics. The EIS results agree well with the electrochemical behaviors.

Table 1. Fitting results of Nyquist plots using the equivalent circuit

Sample	R_s (Ω)	R_1 (Ω)	CPE_1		R_2 (Ω)	CPE_2	
			Y	n		Y	n
ZnO/G 5cycles	3.4	10.1	7.6×10^{-5}	0.94	18.1	3.3×10^{-5}	0.74
ZnO/G 25cycles	3.5	11.0	9.8×10^{-5}	0.88	18.7	2.6×10^{-5}	0.76
ZnO 5cycles	4.5	15.7	1.6×10^{-4}	0.81	10.7	6.3×10^{-5}	0.74
ZnO 25cycles	8.7	13.3	1.4×10^{-4}	0.92	24.2	1.0×10^{-4}	0.67

4. CONCLUSIONS

In summary, ZnO-graphene nanocomposite with a layered structure has been synthesized by a facile in situ hydrothermal route. The ZnO nanoparticles with an average size of around 30-40 nm are uniformly loaded on graphene. The ZnO/graphene nanocomposite shows an improved cycling stability compared to bare ZnO. The improvement in cycling stability is attributed to the introduction of the flexible graphene that acts both as the buffer to alleviate the volume changes and as the separator to refrain the aggregation of the ZnO nanoparticles. The introduction of the graphene also offers a 2D conductive network and increases the specific surface area, leading to the enhanced electrochemical reaction kinetics.

ACKNOWLEDGEMENTS

This work was financially supported by Zijin Program of Zhejiang University, China, the Fundamental Research Funds for the Central Universities (No. 2010QNA4003), the Ph.D. Programs Foundation of Ministry of Education of China (No. 20100101120024), the Foundation of Education Office of Zhejiang Province (No. Y201016484), the Qianjiang Talents Project of Science Technology Department of Zhejiang Province (2011R10021), and the National Natural Science Foundation of China (No. 51101139).

References

1. J. Q. Wang, I. D. Raistrick, and R. A. Huggins, *J. Electrochem. Soc.* 133 (1986) 457.
2. R. A. Huggins, *J. Power Sources* 81-82 (1999) 13.
3. J. Q. Wang, P. King, and R. A. Huggins, *Solid State Ionics* 20 (1986) 185.
4. H. Li, X. J. Huang, and L. Q. Chen, *Solid State Ionics* 123 (1999) 189.
5. F. Belliard, P. A. Connor, and J. T. S. Irvine, *Solid State Ionics* 135 (2000) 163.
6. F. Belliard and J. T. S. Irvine, *J. Power Sources* 97-98 (2001) 219.
7. F. Zhou, X. M. Zhao, H. G. Zheng, T. Shen, and C. M. Tang, *Chem. Lett.* 34 (2005) 1114.
8. H. B. Wang, Q. M. Pan, Y. X. Cheng, J. W. Zhao, and G. P. Yin, *Electrochim. Acta* 54 (2009) 2851.
9. Y. Sharma, N. Sharma, G. V. Subba Rao, and B. V. R. Chowdari, *Adv. Funct. Mater.* 1728 (2007) 2855.
10. Y. Sharma, N. Sharma, G. V. Subba Rao, and B. V. R. Chowdari, *Electrochim. Acta* 53 (2008) 2380.
11. L. F. Xiao, Y. Q. Zhao, J. Yin, and L. Z. Zhang, *Chem. Eur. J.* 15 (2009) 9442.
12. C. Q. Zhang, J. P. Tu, Y. F. Yuan, X. H. Huang, X. T. Chen, and F. Mao, *J. Electrochem. Soc.* 154 (2007) A65.
13. J. P. Liu, Y. Y. Li, X. T. Huang, G. Y. Li, and Z. K. Li, *Adv. Funct. Mater.* 18 (2008) 1448.
14. J. H. Lee, M. H. Hon, Y. W. Chung, and I. C. Leu, *Appl. Phys. A* 102 (2011) 545.
15. J. P. Liu, Y. Y. Li, R. M. Ding, J. Jiang, Y. Y. Hu, X. X. Ji, Q. B. Chi, Z. H. Zhu, and X. T. Huang, *J. Phys. Chem. C* 113 (2009) 5336.
16. X. D. Tang, Q. M. Pan, and J. Liu, *J. Electrochem. Soc.* 157 (2010) A55.
17. K. S. Novoselov, A. K. Geim, S. V. Morozov, D. Jiang, Y. Zhang, S. V. Dubonos, I. V. Grigorieva, and A. A. Firsov, *Science* 306 (2004) 666.
18. M. D. Stoller, S. Park, Y. W. Zhu, J. H. An, and R. S. Ruoff, *Nano Lett.* 8 (2008) 3498.
19. C. Lee, X. D. Wei, J. W. Kysar, and J. Hone, *Science* 321 (2008) 385.
20. S. Park, J. H. An, I. W. Jung, R. D. Piner, S. J. An, X. S. Li, A. Velamakanni, and R. S. Ruoff, *Nano Lett.* 9 (2009) 1593.
21. J. Yao, X. P. Shen, B. Wang, H. K. Liu, and G. X. Wang, *Electrochem. Commun.* 11 (2009) 1849.
22. S. M. Paek, E. Yoo, and I. Honma, *Nano Lett.* 9 (2009) 72.
23. D. H. Wang, R. Kou, D. W. Choi, Z. G. Yang, Z. M. Nie, J. Li, L. V. Saraf, D. H. Hu, J. G. Zhang, G. L. Graff, J. Liu, M. A. Pope, and I. A. Aksay, *ACS Nano* 4 (2010) 1587.
24. X. Y. Wang, X. F. Zhou, K. Yao, J. G. Zhang, and Z. P. Liu, *Carbon* 49 (2011) 133.
25. J. Xie, S. Y. Liu, X. F. Chen, Y. X. Zheng, W. T. Song, G. S. Cao, T. J. Zhu, and X. B. Zhao,
26. *Int. J. Electrochem. Sci.* 6 (2011) 5539
27. S. J. Ding, D. Y. Luan, F. Y. C. Boey, J. S. Chen, and X. W. Lou, *Chem. Commun.* 47 (2011) 7155.
28. L. S. Zhang, L. Y. Jiang, H. J. Yan, W. D. Wang, W. Wang, W. G. Song, Y. G. Guo, and L. J. Wan, *J. Mater. Chem.* 20 (2010) 5462.
29. J. Xie, Y. X. Zheng, R. J. Pan, S. Y. Liu, W. T. Song, G. S. Cao, T. J. Zhu, and X. B. Zhao,

30. *Int. J. Electrochem. Sci.* 6 (2011) 4811.
31. Y. P. Zhang, H. B. Li, L. K. Pan, T. Lu, and Z. Sun, *J. Electroanal. Chem.* 634 (2009) 68.
32. W. S. Hummers and R. E. Offeman, *J. Am. Chem. Soc.* 80 (1958) 1339.
33. F. Tuinstra and J. L. Koenig, *J. Chem. Phys.* 53 (1970) 1126.
34. X. Y. Ye, Y. M. Zhou, Y. Q. Sun, J. Chen, and Z. Q. Wang, *J. Nanopart. Res.* 11 (2009) 1159.
35. P. K. Sharma, M. Kumar, and A. C. Pandey, *J. Nanopart. Res.* 13 (2011) 1629.
36. J. M. Calleja and M. Cardona, *Phys Rev B* 16 (1977) 3753.
37. Z. W. Peng, G. Z. Dai, W. C. Zhou, P. Chen, Q. Wan, Q. L. Zhang, and B. S. Zou, *Appl. Surf. Sci.* 256 (2010) 6814.
38. A. Umar, S. H. Kim, Y. S. Lee, K. S. Nahm, and Y. B. Hahn, *J. Cryst. Growth.* 282 (2005) 131.
39. S. Stankovich, D. A. Dikin, R. D. Piner, K. A. Kohlhaas, A. Kleinhammes, Y. Y. Jia, Y. Wu, S. T. Nguyen, and R. S. Ruoff, *Carbon* 45 (2007) 1558.
40. S. Stankovich, R. D. Piner, X. Q. Chen, N. Q. Wu, S. T. Nguyen, and R. S. Ruoff, *J. Mater. Chem.* 16 (2006) 155.
41. X. F. Guo, J. Jang, and S. Nagase, *J. Phys. Chem. C* 114 (2010) 832.
42. D. Li, M. B. Müller, S. Gilje, R. B. Kaner, and G.G. Wallace, *Nat. Nanotechnol.* 3 (2008) 101.
43. A. Abouimrane, O. C. Compton, K. Amine, and S. T. Nguyen, *J. Phys. Chem. C* 114 (2010) 12800.
44. H. Li, X. J. Huang, and L. Q. Chen, *J. Power Sources* 81–82 (1999) 340.
45. T. Piao, S. M. Park, C. H. Doh, and S. J. Moon, *J. Electrochem. Soc.* 146 (1999) 2794.